The possible role of Reynolds stress in the creation of a transport barrier in tokamak edge plasmas *)

M. Vergote, M. Van Schoor, Y. Xu, S. Jachmich, R. Weynants

Laboratoire de physique des plasmas — Laboratorium voor Plasmafysica, Association 'Belgian State', Ecole Royale Militaire — Koninklijke Militaire School, B-1000 Brussels, Belgium (Partner in Trilateral Euregio Cluster).

M. Hron, J. Stöckel

Institute of Plasma Physics, Association Euratom/IPP.CR, Prague, Czech Republic

Received 31 January 2005

To obtain a good confinement, mandatory in a fusion reactor, the understanding of the formation of transport barriers in the edge plasma of a tokamak is essential. Turbulence, the major candidate to explain anomalous transport, can be quenched by sheared flows in the edge which rip the convective cells apart, thus forming a barrier. Experimental evidence from the Chinese HT-6M tokamak [Y.H. Xu et al.: Phys. Rev. Lett. **84** (2000) 3867], points to the fact that momentum transfer from the turbulence can create these sheared flows via the Reynolds stresses. A new 1-D fluid model for the generation of the poloidal flow, has been developed taking into account the driving force of the Reynolds stress and the friction forces due to neutrals and parallel viscosity. Special attention has been dedicated to the computation of the flux-surface-averaging for the various terms. This model has been confronted with the experimental results obtained in the HT-6M tokamak, where Reynolds stresses were generated by application of a turbulent heating pulse. If the model is applied in cylindrical geometry, the calculated Reynolds stress-induced flow agrees well with the measured poloidal velocity in the plasma edge. However, when the full toroidal geometry is taken into account, it seems that the Reynolds stresses are too small to explain the observed rotation. This indicates that the role of the Reynolds stresses in inducing macroscopic flow in the torus is weakened. A combined system of probes allowing to measure the Reynolds stress and the rotation velocity simultaneously, has been developed and installed on the CASTOR tokamak (Prague). We report here on the first results obtained.

PACS: 52.35.Ra
Key words: Reynolds stress, turbulence, anomalous transport, rotation

1 Introduction

H-mode physics and the creation of transport barriers are important issues in our quest to build a fusion reactor as they are indeed directly related to the magnitude and the control of the losses due to the radial transport of the plasma. The radial transport cannot be explained without duly taking into account the ever present turbulence. The paradigm that losses due to turbulence can be reduced

*) Presented at the Workshop "Electric Fields Structures and Relaxation in Edge Plasmas", Nice, France, October 26–27, 2004.

by the creation of sheared flows in the plasma, is long standing and has been investigated by many researchers [1–3]. A shear flow can indeed rip the turbulent cells apart, thus reducing the micro-convection which is at the origin of turbulent losses. In recent years however, attention has been focused on the inverse process in which the turbulence also influences the mean flow by means of Reynolds stresses. These stresses can transfer momentum from the mean flow towards the turbulence, a process which is at the basis of the so-called anomalous viscosity; but they can also transfer momentum from the turbulence towards the mean flow, as has been shown by Xu et al. [4]. Furthermore, the non-linear convection term in the momentum equation, which is at the origin of the Reynolds stress, is also responsible for the transfer of momentum from one range in the turbulence's spectrum towards another, giving eventually rise to zonal flows. When these processes take place in a limited region of the plasma, sheared flows are created locally, influencing on their turn again the turbulence and a self-regulating equilibrium might be created.

In this paper, we propose to study these processes in more detail by a comparison between theory and experiment. We start in Section 2 by presenting a new one-dimensional model, which includes the Reynolds stress term. In Section 3, a simulation based on this model is compared to the experimental observations at HT-6M and CASTOR. In Sections 4 and 5 we present some secondary results of the campaign, which was held in CASTOR.

2 Modelling of the poloidal acceleration due to Reynolds stress

We start from the Braginskii equations [5] and follow the method originally proposed by Reynolds and used by Peeters [6], writing the fluid velocity $\vec{v}$ and the density n as a mean plus a fluctuating part ($\vec{v} = \underline{\vec{v}} + \underset{\sim}{\vec{v}}$, $n = \underline{n} + \underset{\sim}{n}$). The mean is defined as a time-average $\underline{x} = \langle x \rangle_\tau = (1/\tau) \int_t^{t+\tau} x \, \mathrm{d}t$ with τ (the timescale of averaging) large compared to the timescale of the fluctuations, but short with respect to any macroscopical timescale. Defining the total velocity $\vec{U} = \underline{\vec{v}} + \underline{\underset{\sim}{n}\underset{\sim}{\vec{v}}} / \underline{n}$, the total momentum equation (the sum of the electron and ion momentum equations) takes the form

$$m \frac{\partial}{\partial t}(\underline{n}\vec{U}) + m \vec{\nabla}.(\underline{n}\vec{U}\vec{U}) + m \vec{\nabla}.(\underline{n}\underline{\underset{\sim}{\vec{v}}\underset{\sim}{\vec{v}}}) + \underline{\vec{\nabla}.\vec{\vec{P}}} = \underline{\vec{J}} \times \vec{B} - m(\underline{n}\nu^*)\vec{U} \qquad (1)$$

in which $\vec{\nabla}.(\underline{n}\underline{\underset{\sim}{\vec{v}}\underset{\sim}{\vec{v}}})$ is the Reynolds stress term and $m(\underline{n}\nu^*)\vec{U}$ is the neutral friction force with $\underline{n}\,\underline{\nu^*} = \underline{n}(n_{\mathrm{neutrals}} \langle \sigma.v \rangle) = \nu$ the neutral friction coefficient [7]. The other symbols have their usual meaning.

Using the same technique, it is possible to write the continuity equation in the form $\partial_t \underline{n} + \vec{\nabla}.(\underline{n}\vec{U}) = 0$. Expressing this equation in toroidal coordinates ((r, θ, φ), denoting the radial, poloidal and toroidal coordinates, respectively), one can define the flux-surface-average poloidal rotation $\langle U_\theta \rangle_{\mathrm{flux}} = F(r)/R_0$ (where the flux-surface-average of a quantity X is $\langle X \rangle_{\mathrm{flux}} = (1/2\pi R_0 \, 2\pi r) \int_\varphi \int_\theta X \, r \mathrm{d}\theta \, R \mathrm{d}\varphi$) and write the poloidal velocity as $U_\theta = (R_0/R)F(r)/R_0$, where R is the major radius and R_0 the major radius at the magnetic axis.

From the toroidal and parallel components of Eq. (1) we can write an equation for $F(r)$ [8]:

$$\frac{\partial}{\partial t}\left(\frac{F(r)}{R_0}\right) = \frac{B_0}{\underline{n}\, m\,(1+2q^2)}\,\langle\, J_r\,\rangle_{\rm flux} - \frac{1+\frac{1}{2}\varepsilon^2}{\underline{n}\,(1+2q^2)}\frac{1}{r^2}\frac{\partial}{\partial r}\left(r^2\,\underline{n\tilde{v}_r\tilde{v}_\theta}\right) - \nu^*\frac{F(r)}{R_0} - \frac{1+\frac{3}{2}\varepsilon^2}{\underline{n}\Theta m B_0(1+2q^2)}C\left(\frac{F(r)}{R_0} - U_{\rm Neo}\right). \qquad (2)$$

In this equation, the convection has been neglected and the viscosity is reduced to $\langle \vec{B}.\vec{\nabla}.\vec{\pi}\rangle_{\rm flux} = C(F(r)/R_0 - U_{\rm Neo})$ where for the collisional regime $C = B_0\frac{3}{2}\Theta\eta_0/R_0^2$ and $U_{\rm Neo} = (-2.1/Ze\,B_0)(\partial T_i/\partial r)$ [8]. Furthermore we have $\Theta = \tan\alpha$, with α the pitch of the magnetic field, $\varepsilon = r/R_0$ the inverse aspect ratio and $q = \varepsilon/\tan\alpha$ the safety-factor.

The turbulence is supposed to be electrostatic, so that $\tilde{\vec{v}} = (1/B^2)(\vec{B}\times\vec{\nabla}\tilde{\phi})$. An important consequence of this statement, is that $\tilde{v}_\parallel = 0$, so that $\tilde{v}_\varphi = -\Theta\,\tilde{v}_\theta$, resulting finally in a rather simple form for the Reynolds stress term in Eq. (2). Expressed in the reference frame (r,θ,φ), the Reynolds stress tensor from Eq. (1) takes the following form:

$$\underline{n\tilde{\vec{v}}\tilde{\vec{v}}} = \underline{n}\begin{pmatrix} \underline{\tilde{v}_r^2} & \underline{\tilde{v}_r.\tilde{v}_\theta} & \underline{\tilde{v}_r.\tilde{v}_\varphi} \\ \underline{\tilde{v}_\theta.\tilde{v}_r} & \underline{\tilde{v}_\theta^2} & \underline{\tilde{v}_\theta.\tilde{v}_\varphi} \\ \underline{\tilde{v}_\varphi.\tilde{v}_r} & \underline{\tilde{v}_\varphi.\tilde{v}_\theta} & \underline{\tilde{v}_\varphi^2} \end{pmatrix}$$

$$\approx \underline{n}\begin{pmatrix} \overline{(-\nabla_\theta\tilde{\phi})^2} & \overline{-(\nabla_r\tilde{\phi}\nabla_\theta\tilde{\phi})} & \overline{\Theta(\nabla_r\tilde{\phi}\nabla_\theta\tilde{\phi})} \\ \overline{-(\nabla_r\tilde{\phi}\nabla_\theta\tilde{\phi})} & \overline{(\nabla_r\tilde{\phi})^2} & \overline{-\Theta(\nabla_r\tilde{\phi})^2} \\ \overline{\Theta(\nabla_r\tilde{\phi}\nabla_\theta\tilde{\phi})} & \overline{-\Theta(\nabla_r\tilde{\phi})^2} & \overline{\Theta^2(\nabla_r\tilde{\phi})^2} \end{pmatrix}\frac{\cos^2\alpha}{B^2},$$

in which the elements on the third row and the third column are negligibly small, compared to the others, because Θ is of the order of 10^{-2}. The remaining four elements can be interpreted statistically as the two variances $\underline{\tilde{v}_r^2} \approx \overline{(-\nabla_\theta\tilde{\phi}/B)^2}$ and $\underline{\tilde{v}_\theta^2} \approx \overline{(\nabla_r\tilde{\phi}/B)^2}$ and the covariance between the signals $v_r(t)$ and $v_\theta(t)$: $\overline{(\underline{\tilde{v}_r\tilde{v}_\theta})}$.

Equation (2) can be compared to the results mentioned by Diamond et al. [9] and used in [4]:

$$\frac{\partial v_\theta}{\partial t} = -\frac{\partial}{\partial r}\left(\underline{\tilde{v}_r\tilde{v}_\theta}\right) - \mu v_\theta. \qquad (3)$$

In this equation, the Reynolds stress alone drives the poloidal rotation through its radial gradient, while all damping terms are grouped together in one coefficient μ. It is clear that Eq. (2) presents some interesting new features. First of all, we can confirm the role of the Reynolds stress as eventual driving term, but loosing importance by the factor $(1+2q^2)$, which appears by correctly taking into account the geometry of the machine, but which is in most edge plasmas of tokamaks larger than 10 (In the case of CASTOR we have in the edge $q > 8$). Moreover, Eq. (2) gives us an expression of the friction coefficient μ and can be used to compare the various

mechanisms to damp poloidal rotation (viscosity and neutral friction). Finally, one can use Eq. (2) to compare various scenarios with respect to how poloidal rotation is created: by applying a radial current or by a radial gradient in the Reynolds stress.

3 Comparison of model simulations with measurements at HT-6M, CASTOR, and ISTTOK

3.1 Comparison with measurements at HT-6M

We confronted our model first with turbulent heated experiments at HT-6M, during which Reynolds stress was almost continuously measured. We used the global parameters of the shots and the measured Reynolds stresses, given by Xu et al. in [4], to see what kind of poloidal rotation we could predict by our model, Eq. (2). In HT-6M, the transition causing an improved confinement, was induced by a turbulent heating (TH) pulse. This TH-pulse causes a large amount of turbulence, as can be seen in the measurements of the Reynolds stress-profiles. These profiles, recorded on a shot-to-shot basis [4], show a clear steepening immediately after the start of the turbulent heating pulse ($t = 0$), as seen in Fig. 1.

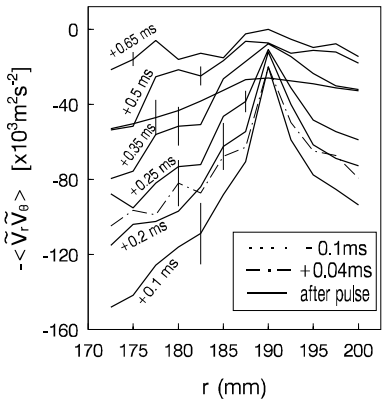

Fig. 1. Measured Reynolds stress profiles in HT-6M just before and after the TH-pulse.

According to Eq.(2), this gradient of the Reynolds stress can cause an acceleration in the poloidal direction. Then we used the measured values of the Reynolds stress from Fig. 1 to calculate the poloidal velocity with our model, starting from the known profile at $t = 0$, but we found only non-negligible contributions of the Reynolds stress in the accelerating zone when we took $q = 0$ in the Reynolds stress term of Eq. (2). In Fig. 2a the radial profile evolution of the poloidal velocity is shown for this case $q = 0$. For these simulations we further took $\langle J_r \rangle_{\text{flux}} = 0$ and a neutral density at the separatrix of 1 % of the ion density, decreasing inwards with a decay length of 1 cm.

However, when the real value of q ($q(a) \approx 6$) is used in the Reynolds stress term, we find a small acceleration in this area ($0.18\,\text{m} < r < 0.187\,\text{m}$) and we cannot reproduce the measured profiles there (see Fig. 2b). Our model is more satisfactory

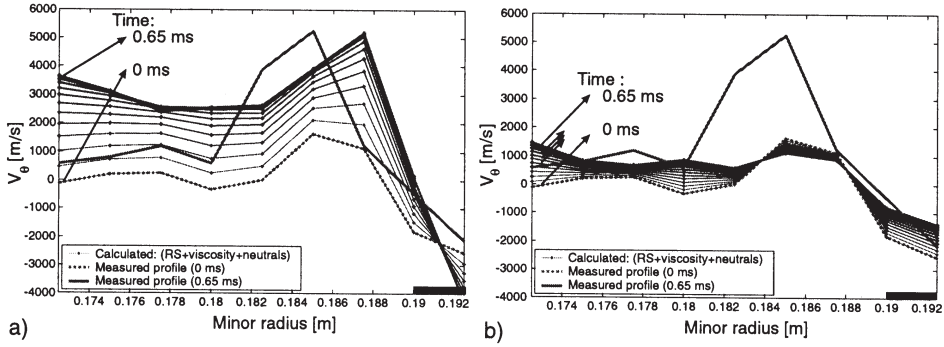

Fig. 2. a) Consecutive profiles of the poloidal velocity in HT-6M, as modelled by Eq. (2) with $q = 0$. b) Model simulations, with the measured q-value.

deeper inside, where no significant acceleration is seen: for $r < 0.18\,\mathrm{m}$, the simulated end-velocity corresponds rather good to the measured poloidal velocities at 0.65 ms. The discrepancy close to the limiter, is possibly due to the poloidal limiter in HT-6M, or to the too big amount of turbulence, created by the TH-pulse and penetrating $\approx 1\,\mathrm{cm}$ in the plasma inside the limiter. As a result of this, one could doubt the real value of q in this region, as the magnetic field lines are intersected by the limiter or too much disturbed by the TH-pulse. Also the concept of flux surface averaging can be questioned close to the last closed flux surface (LCFS).

The last profiles, shown in Fig. 2 are represented at $t = 0.65\,\mathrm{ms}$. After 0.65 ms, the Reynolds stress becomes negligible, which causes the poloidal rotation to decay because of the friction terms. The previous analysis was impeded due to the lack of precise quantitative measurements of the poloidal rotation in HT-6M.

3.2 Measurements at CASTOR

To get more reliable and independent measurements of the Reynolds stresses and of the flow velocities and to investigate the relation between them, a Gundestrup-probe and a Reynolds stress-probe were mounted in CASTOR on the same forked manipulator (Fig. 3). Ohmic shots as well as electrode-polarized shots in an hydrogen-plasma were performed with the following typical machine parameters: $a = 85\,\mathrm{mm}$, $R_0 = 400\,\mathrm{mm}$, $B_0 = 1.3\,\mathrm{T}$, $I_\mathrm{p} = 8\,\mathrm{kA}$, $q(a) = 15$. In this non-biasing regime, the line averaged plasma density is of the order of $8 \times 10^{18}\,\mathrm{m}^{-3}$, and during the biasing phase $2 \times 10^{19}\,\mathrm{m}^{-3}$.

The Reynolds stress-probe has 7 Langmuir probe-pins arranged in 2 rows as shown in Fig. 3 (the "downstream" row with pins $1, 3, 5$, and 7 and the "upstream" row with pins $2, 4$ and 6, of which pins 2 and 4 are raised by 3 mm. Within the rows the pins are spaced by a poloidal distance of 2.5 mm).

The signals are sampled at a frequency of 1 MHz. Pins 1–2–3 and 3–4–5 are used for Reynolds stress measurements, pins 5–6–7 are used as a triple-probe to determine the temperature and the density.

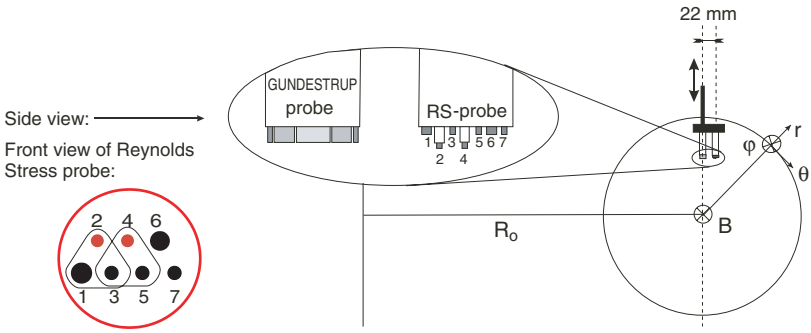

Fig. 3. Schematic drawing of the experimental setup at Castor.

The Reynolds stress $\underset{\sim}{v_r v_\theta} = \langle -\nabla_\theta \underset{\sim}{\phi} \nabla_r \underset{\sim}{\phi} / B^2 \rangle_\tau$ is computed at the center of the triangle (1–2–3) as

$$RS_{(123)} = \left\langle -\frac{1}{B^2} \left(\frac{(\underset{\sim}{\phi}_{fl,3} - \underset{\sim}{\phi}_{fl,1})}{r\Delta\theta} \frac{(\underset{\sim}{\phi}_{fl,(13)} - \underset{\sim}{\phi}_{fl,2})}{\Delta r} \right) \right\rangle_\tau$$

with $\underset{\sim}{\phi}_{fl,(13)} = \frac{1}{2}(\underset{\sim}{\phi}_{fl,1} + \underset{\sim}{\phi}_{fl,3})$ being the average potential of pin 1 and 3. For the second combination of pins 3,4 and 5, we have

$$RS_{(345)} = \left\langle -\frac{1}{B^2} \left(\frac{(\underset{\sim}{\phi}_{fl,5} - \underset{\sim}{\phi}_{fl,3})}{r\Delta\theta} \frac{(\underset{\sim}{\phi}_{fl,(35)} - \underset{\sim}{\phi}_{fl,4})}{\Delta r} \right) \right\rangle_\tau .$$

Because of the off-axis position of the Reynolds stress-probe (due to the width of the fork of the manipulator of 22 mm) and the poloidal distance between the measurement points 1–2–3 and 3–4–5, these measurements are not taken at the same

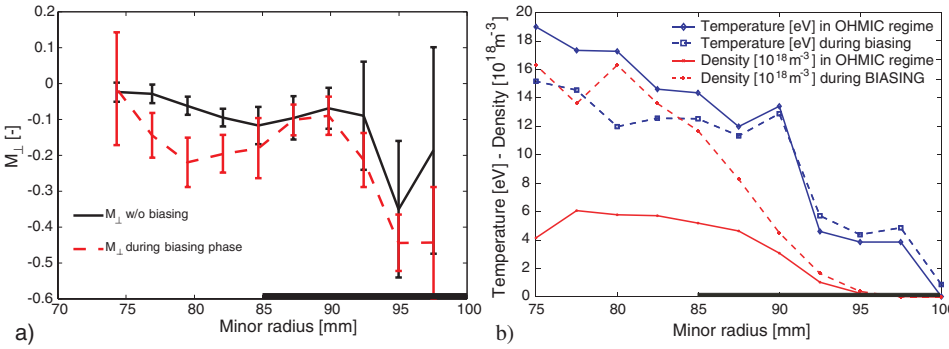

Fig. 4. a) Perpendicular Mach number, measured by the Gundestrup-probe, and b) density and temperature profiles.

minor radius, so that the gradient of the Reynolds stress is given by $|\vec{\nabla}_r(RS)| = (RS_{(345)} - RS_{(123)})/\Delta r$, where $\Delta r = 52/r$ [mm], r being the minor radius at the middle position of the Reynolds stress-probe.

Simultaneous measurements of the poloidal and parallel flow velocity, were performed with an ideal Gundestrup-probe [10], with 8 collectors [11], placed on the same manipulator, of which the radial position can be changed on a shot-to-shot basis, and which is inserted in the plasma at the top of the tokamak.

In the biasing shots, the electrode was mounted at $r_{\mathrm{electrode}} = 75\,\mathrm{mm}$ (radial extent of electrode $= 5\,\mathrm{mm}$), toroidally 180° away from the 2 probes, and applied from $t = 10\,\mathrm{ms}$ on, a positive voltage of 200 V on the plasma. Typical $M_\perp$-profiles, as well as T_e- and n_e-profiles before (at $t = 9.5\,\mathrm{ms}$) and during biasing (late in the biasing phase, at $t = 14.5\,\mathrm{ms}$) are shown in Fig. 4.

3.3 Comparison between model simulations and measurements at CASTOR

We can now again analyse the importance of the Reynolds stress as a source of poloidal rotation. We limit the analysis to ohmic shots, since during the biasing phase the role of the Reynolds stress is overwhelmed by the radial current. Figure 5 shows a typical radial profile of the Reynolds stress (Fig. 5a) and its gradient (Fig. 5b), calculated in two different ways for such an ohmic scenario. The dotted line shows the gradient computed as the difference between the measurements of the Reynolds stress at the triplets (123) and (345) (which are at a slightly different radial location). The full black line is the radial derivative of the mean of the light

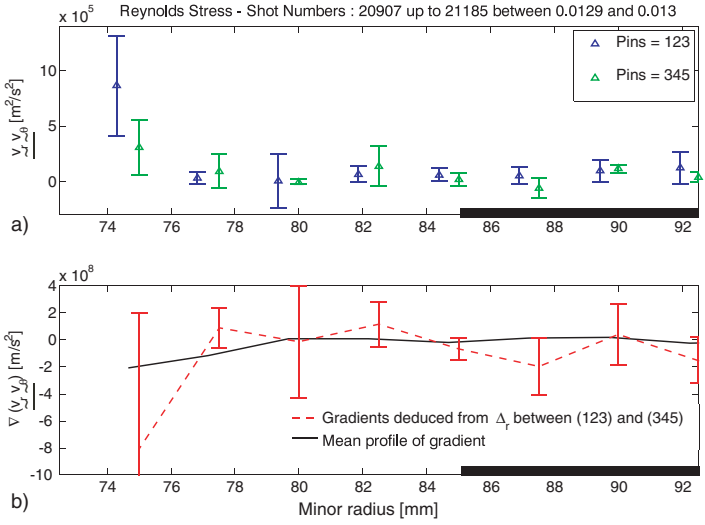

Fig. 5. a) A snapshot of Reynolds stress measurements by the two different triplets (123) and (345), at $t = 12.9\,\mathrm{ms}$. b) Radial gradient of Reynolds stress, computed in 2 different ways in ohmic discharges.

and the dark dots of Fig. 5a, being the average of all individual measurements of the Reynolds stress at that radius. The error-bars on the plots are obtained by comparing several reproducible shots. Note that the Reynolds stresses are of the same order of those measured in HT-6M [4], but the gradient is less pronounced and the error-bars are more important. The gradient develops a few millimeters inside the separatrix; the error-bars in this region are also the largest.

We then apply the model presented in Eq. (2) and obtain the results shown in Figs. 6a,b for both approaches for the estimation of the gradient, using the real values of q and supposing a neutral density of 10^{16} m^{-3} everywhere. Note that Fig. 5 only shows a snapshot of the Reynolds stress, while Fig. 6 uses these different actual values of the Reynolds stress between 12 and 13 ms to compute the poloidal velocity profile as a function of time.

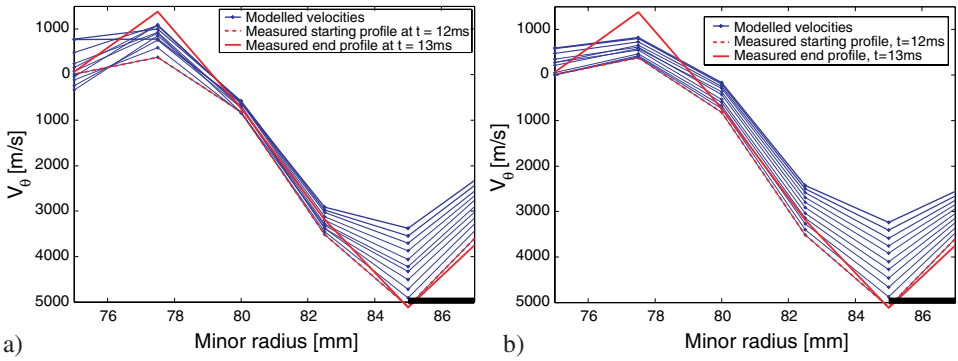

Fig. 6. Poloidal velocities, simulated by Eq. (2), starting from the measured profile at $t = 12$ ms with the measured q-values and with a) the gradients of the Reynolds stress derived within one shot (dotted line in Fig. 5b) and b) the mean gradient derived from shot to shot (full black line in Fig. 5b).

Whatever definition of the gradient is used, we see a clear damping of the flow close to the separatrix. However, in both cases, the flow is accelerated more inside. This acceleration can only be due to the Reynolds stress. Moreover, to obtain this result we took the real value of q ($q(a) \approx 15$), and used the different dotted (a) or full black (b) profiles from Fig. 5 at the subsequent times. If q is taken equal to zero, we obtain accelerations that are two orders of magnitude too high and that cannot be damped by increasing the neutral density as then the damping close to the separatrix would be far too high, so that the flows would be reduced to zero over the simulated period of time. Therefore, we tend to conclude that the factor of $1 + 2q^2$ seems to be justified in this case. Other values of q are unfortunately not available at this moment for further investigation. The only difference between the two plots Figs. 6a and b is that the Reynolds stress-gradient in the case of (b) is less able to compensate the damping due to the neutrals and the viscosity, close to the separatrix ($r \geq 80$ mm).

3.4 Equivalent radial current

To decide whether the Reynolds stress could be responsible for an L to H-mode transition, we compared the effects of $\langle J_r \rangle_{\text{flux}}$ (eg. during a L–H transition in TEXTOR) and of the gradient of the Reynolds stress $\langle \partial_r(\underline{v_r v_\theta}) \rangle_{\text{flux}}$. We transformed the Reynolds stress-gradient into an equivalent radial current density $\langle J_r \rangle_{\text{flux}}$, causing the same acceleration. This radial current can be made dimensionless [12] so that different machines can be compared. Table 1 represents the values of Reynolds stress measured in HT-6M [4], ISTTOK [13] and CASTOR, and the radial current typically drawn by a biasing electrode in H-mode operation in TEXTOR [8].

Table 1. Comparison of the equivalent radial current densities among different machines.

	$2\pi a \cdot 2\pi R_0$ (m^2)	$\partial_r\left(\underline{v_r v_\theta}\right)$ (m/s^2)	Equivalent current density $\langle J_r \rangle_{\text{flux}} \equiv \frac{I_{r,\text{bias}}}{2\pi a \cdot 2\pi R_0}$ (A/m^2)	$I^* = \frac{J_r 2\pi a\, B_0}{\underline{n} m C_s^2}$ (–)
HT-6M	5	10^7	0.025	2.6×10^{-3}
ISTTOK	1.5	10^8	0.17	15×10^{-3}
CASTOR	1.34	2×10^8	2.5	30×10^{-3}
TEXTOR	28.5	–	4.5	0.25

It can be clearly seen that all the equivalent dimensionless currents, are of the same order of magnitude and significantly lower than the radial current drawn by the biasing electrode in TEXTOR. It is clear that the driving force due to the Reynolds stress is much smaller than the driving force needed in TEXTOR to obtain a bias induced transition. As such it seems doubtful that Reynolds stresses can be solely responsible for a L–H transition.

4 Reynolds stress properties

In order to search for a possible influence of the edge-biasing on the Reynolds stress properties, we investigate the behavior of the Reynolds stress during an L–H transition in CASTOR, where in the polarization experiments a positive voltage, starting from $t \approx 10\,\text{ms}$, was applied by an electrode located at $r = 75\,\text{mm}$. The current density drawn by the electrode during the biasing phase is above $20\,\text{A/m}^2$. The Reynolds stress has been measured continuously through the different imposed transition scenarios, ranging from an almost sudden ramp-up biasing voltage (step-function) to one, very slowly ramping up.

An interesting scenario is shown in Fig. 7 for the case of a slowly ramping up biasing experiment, in which the Reynolds stress is measured at $r = 82.5\,\text{mm}$.

From Fig. 7a, one sees that the Reynolds stress magnitude is modified during the biasing phase. The different components of the Reynolds stress, i.e., $\langle \underset{\sim}{v}_r^2 \rangle =$

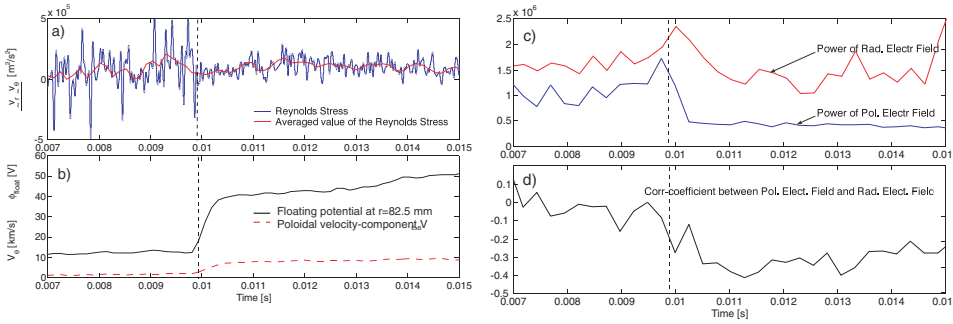

Fig. 7. a) Reynolds stress behavior during the biasing phase, measured at $r = 82.5\,\mathrm{mm}$. b) Poloidal velocity and floating potential. c) Power of the individual signals $\langle \underset{\sim}{v}_r^2 \rangle$ and $\langle \underset{\sim}{v}_\theta^2 \rangle$. d) Correlation coefficient between $\underset{\sim}{v}_r$ and $\underset{\sim}{v}_\theta$.

$\langle (\underset{\sim}{E}_\theta/B)^2 \rangle$, $\langle \underset{\sim}{v}_\theta^2 \rangle = \langle (-\underset{\sim}{E}_r/B)^2 \rangle$ and $\langle \underset{\sim}{v}_r \underset{\sim}{v}_\theta \rangle / \sqrt{\langle \underset{\sim}{v}_r^2 \rangle \langle \underset{\sim}{v}_\theta^2 \rangle}$ are linked to the power of the poloidal and radial fluctuating electric field and to the cross correlation of both respectively, which are represented in Fig. 7c and d. In Fig. 7c, one can see that during biasing $\langle \underset{\sim}{v}_r^2 \rangle$ is reduced significantly, while changes in $\langle \underset{\sim}{v}_\theta^2 \rangle$ are rather small. Meanwhile, the cross-correlation coefficient, $\langle \underset{\sim}{v}_r \underset{\sim}{v}_\theta \rangle / \sqrt{\langle \underset{\sim}{v}_r^2 \rangle \langle \underset{\sim}{v}_\theta^2 \rangle}$ changes considerably (Fig. 7d).

It should be noted that on other radii, the effect of the bias on the various components of the Reynolds stress, can be different. We see very often a decrease in amplitude, while the effect on the correlation is not everywhere seen. Furthermore, we observed that the fluctuation amplitude of the radial electric field is always (this is the case for almost every r) larger than that of the poloidal electric field, which means that the fluctuations in the poloidal velocity are more important than those in the radial velocity, as seen in Fig. 7c. The contributions to the electrostatic Reynolds Stress come thus in amplitude mostly from the fluctuating poloidal velocities.

5 Cross-bicoherence between both components of Reynolds stress and the poloidal velocity

Whereas the original goal was to study the influence the Reynolds stress could have on zero-frequency large scale poloidal rotation, we now extend our study to low-frequency zonal flows (ZF, $k_r \gg k_\theta$) interacting with the Reynolds stress. This problem can be treated as a three-wave interaction, which has been studied by several authors [14, 15]. The first two high frequency fluctuations ($x = \underset{\sim}{v}_r$ and $y = \underset{\sim}{v}_\theta$) come from the Reynolds stress. We take the third one, supposed to be a low-frequency wave, as the fluctuating radial electric field ($z = \underset{\sim}{E}_r$). As mentioned in [15], the frozen flow hypothesis is also verified in our case. The cross-bicoherence

between the signals $x(t)$, $y(t)$, and $z(t)$ is defined by

$$b^2_{f_3}{}^{XYZ}(f_1, f_2) = \frac{\left|\left\langle Z^*_{f_3=f_1\pm f_2} X_{f_1} Y_{f_2}\right\rangle\right|^2}{\left\langle |Z_{f_3}|^2\right\rangle \left\langle |X_{f_1} Y_{f_2}|^2\right\rangle}$$

and represents the phase coherence between the signals $x(t)$, $y(t)$, and $z(t)$ at the frequencies f_1, f_2, and $f_3 = f_1 \pm f_2$, respectively. Here $X(f)$, $Y(f)$, and $Z(f)$ are the spectral components from respectively the radial and the poloidal velocity and the zonal flow. In addition, one can calculate the total bicoherence $B^2_{f_3} = \sum_{\substack{f_1, f_2 \\ f_3 = f_1 \pm f_2}} b^2_{f_3}(f_1, f_2)$, which gives a measure of the coherent three-wave coupling for all frequencies of f_3, where the sum takes into account all contributions at the couples f_1 and f_2 satisfying $f_1 \pm f_2 = f_3$. Figure 8 shows a plot of the total bicoherence in an ohmic discharge, at radial position $r = 75\,\mathrm{mm}$.

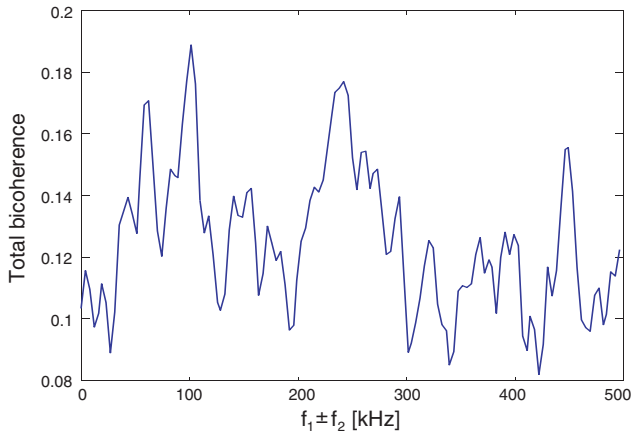

Fig. 8. Total bicoherence for shot number 21178, taken at $t = 11\,\mathrm{ms}$.

The figure clearly shows that there exist several peak structures in the total bicoherence at various frequencies. This result indicates an existence of strong three-wave interaction between the Reynolds stress and the zonal flow on CASTOR. Further identification on this aspect is under the way.

6 Conclusions

We derived a 1D-model for the poloidal acceleration due to the electrostatic Reynolds stress, which takes correctly into account the geometry of the machine. The comparison between the present model (Eq. (2)) and the experimental results on HT-6M and CASTOR tokamaks indicate that the model seems to be valid in the inner edge region of tokamaks. However, nearby the LCFS, the model is not in

agreement with results obtained in HT-6M, unless $q = 0$ is assumed. This leaves doubts on the applicability of the model in the area close to the LCFS, where the value of q is less clear and where the flux surface averaging procedure can even be questioned. Experimental studies on CASTOR have furthermore shown that

(i) under certain conditions in the ohmic discharges, large gradients of Reynolds stress are present, which may play an important role;
(ii) the equivalent current in CASTOR (as well as in HT-6M and ISTTOK) is much lower than that in TEXTOR during a bias-induced transition;
(iii) different influences of sheared poloidal flow on various Reynolds stress components have been observed during biasing discharges;
(iv) there exist strong three-wave interactions between the Reynolds stress and the zonal flow on CASTOR.

The work is partially supported by the project 202/03/0786 of the Grant Agency of the Czech Republic.

References

[1] H. Biglari et al.: Phys. Fluids B **3** (1990) 1626.
[2] K.C. Shaing: Phys. Fluids B **5** (1993) 2122.
[3] S. Jachmich et al.: Plasma Phys. Control. Fusion **40** (1998) 1105.
[4] Y.H. Xu et al.: Phys. Rev. Lett. **84** (2000) 3867.
[5] S.I. Braginskii: *Transport processes in a plasma*, Reviews of Plasma Physics, 1, 1965.
[6] A.G. Peeters: Phys. Plasmas **5** (1998) 763.
[7] M. Harrison: *Physics of plasma-wall interactions in controlled fusion*, NATO ASI of Series B 131, New York, Plenum Press, 1986.
[8] J. Cornelis et al.: Nucl. Fusion **34** (1994) 171.
[9] P.H. Diamond et al.: Phys. Fluids B **3** (1991) 1626.
[10] J. Gunn et al.: Czech. J. Phys. **51** (2001) 5163.
[11] H. Van Goubergen: Ph. D. thesis, Universiteit Gent, 2000.
[12] A. Chankin and P. Stangeby: Plasma Phys. Control. Fusion **38** (1996) 1879.
[13] C. Hidalgo: Phys. Rev. Lett. **83** (1999) 2203.
[14] P.H. Diamond et al.: Phys. Rev. Lett. **84** (2000) 4842.
[15] G.R. Tynan et al.: Phys. Plasmas **8** (2001) 2691.